Chinese Journal of Structural Chemistry

ARTICLE

# $ZnMn_3O_7$: A New Layered Cathode Material for Fast-Charging Zinc-Ion Batteries

Ruitao Sun[1,2], Qin Liu[1,2] and Wenzhuo Deng[1]*

[1]*CAS Key Laboratory of Design and Assembly of Functional Nanostructures, and Fujian Key Laboratory of Nanomaterials; State Key Laboratory of Structural Chemistry, Fujian Institute of Research on the Structure of Matter, Chinese Academy of Sciences, Fuzhou 350002, China*

[2]*University of Chinese Academy of Sciences, Beijing 100039, China*

**ABSTRACT** Low-cost and high-energy-density manganese-based compounds are promising cathode materials for rechargeable aqueous zinc-ion batteries (AZIBs), however, they often experience cycling instability issues and inferior rate capability. Herein, we report a new layered manganese-based cathode material, $ZnMn_3O_7$ (ZMO), which possesses a large interlayer spacing of 4.8 Å and allows the intercalation of ~1.23 Zn-ions per formula unit (corresponding to a capacity of ~170 mAh/g). Importantly, ZMO exhibits good cycling stability (72.9% capacity retention over 400 cycles), ultrafast-charging capability (73% state of charge in 1.5 min), and an ultrahigh power density (3510 W/kg at 88 Wh/kg). Through kinetic characterization, the favorable diffusion of ions and the dominant capacitor contribution are found to be conducive to the achievement of superior fast charging capability. Furthermore, the charge storage mechanism is revealed by ex-situ XRD and ex-situ XPS. This work may shed light on the design of high-performance electrode materials for AZIBs.

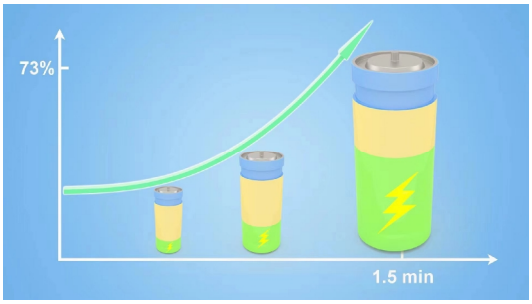


**Keywords:** layered structure, zinc-manganese oxide, cathode, zinc-ion battery

## n INTRODUCTION

The continuous consumption of fossil fuels leads to increasingly serious global environmental problems, so the exploration and utilization of renewable energy are of vital importance.[1-2] However, clean energy resources such as wind energy, solar energy, and tidal energy are greatly affected by the natural climate, and have to be harvested by large-scale energy storage systems so as to meet the large power demand of human society.[3-5] With the development of lithium-ion battery technology, this problem has been resolved, although incompletely. Shortcomings of widely used lithium-ion batteries emerge, such as the surging price and limited lithium reserves,[6-7] and thus the development of new battery technologies to replace lithium-ion batteries is an urgent need.[8] AZIBs have received a lot of attention due to the inherent advantages of metallic zinc anode:[9-12] low cost owing to the abundant natural resource, facile large-scale production, non-toxicity, high theoretical capacity (820 mAh/g) provided by two-electron redox, and the good compatibility with mild acid aqueous electrolytes.

At present, a great number of efforts have been made on cathode materials for AZIBs. As favorable $Zn^{2+}$ (de)embedding hosts, vanadium-based materials[13-23] deliver high specific capacity (>300 mAh/g) and excellent cycling stability, but they could only provide low voltages (less than 0.9 V). Prussian blue analogues[24-32] possess high operating voltages (~1.7 V), however, the low specific capacity (60 mAh/g) limits their development in AZIBs. Manganese oxides have been widely used as cathode materials in primary and secondary batteries[33-34] for energy storage and conversion applications due to their high natural abundance, low toxicity, low cost, relatively high discharge voltage, and high energy density.[10,35-39] For example, the $Zn/MnO_2$ system offers a high specific capacity (a theoretical specific capacity of 308 mAh/g with one electron transferring), a high voltage (~1.3 V), and thus a high energy density. $MnO_2$ exists in a variety of crystalline forms ranging from *α*-, *β*-, *δ*-, *R*-, *γ*-, *λ*-, to *ε*-type, bearing significant structural flexibility.[36] Recent studies have shown that $Mn_3O_4$, $Mn_2O_3$, MnO, and $ZnMn_2O_4$ also exhibit decent $Zn^{2+}$ ions storage capability.[40-43] However, as a result of the complex structure transformation, disproportionation reactions, and the low electronic conductivity, Mn-based materials suffer from severe capacity decay as well as poor rate performance during cycling in mild electrolytes containing pure $Zn^{2+}$ salt.[14,36] Liu et al. proposed a mixed aqueous $ZnSO_4$ + $MnSO_4$ electrolyte.[44] Chen et al. adopted an aqueous $Zn(CF_3SO_3)_2$ electrolyte with $Mn(CF_3SO_3)_2$ additive.[45] The pre-added $Mn^{2+}$ salt inhibits the dissolution of $Mn^{2+}$ from $Mn^{3+}$ so as to improve structural stability and thus increases the capacity retention. Their results show that the cycling performance of the aqueous $Zn/MnO_2$ battery was considerably enhanced. Currently, the development of AZIBs is still in the early stage, and the exploration of new manganese-based materials seems imperative for achieving low-cost and high-performance AZIBs.

In this study, we report a new layered zinc-manganese oxide $ZnMn_3O_7$ (ZMO) as a new cathode material for AZIBs, which could be produced at a notably reduced cost due to the use of abundant elements. Moreover, the manufacturing of ZMO is simple and scalable. The obtained ZMO delivers a high specific capacity of 170.2 mAh/g and an average discharge voltage of 1.35 V at a current density of 200 mA/g. Meanwhile, ZMO exhibits good cycling stability (72.9% capacity retention over 400 cycles at 500 mA/g), and achieves ultrafast-charging capability (73%




DOI: 10.14102/j.cnki.0254-5861.2022-0092

state of charge in 1.5 min) and an ultrahigh power density (3510 W/kg at 88 Wh/kg). In addition, the reaction kinetics were investigated via a couple of electrochemical characterizations, and the underlying reaction mechanism was elucidated by ex-situ X-ray powder diffraction (XRD) and ex-situ X-ray photoelectron spectroscopy (XPS) studies.

## n RESULTS AND DISCUSSION

The XRD pattern along with the Rietveld refinement of the synthesized ZMO sample is illustrated in Figure 1a. All XRD peaks are consistent with the standard pattern of a trigonal crystal system $ZnMn_3O_7$ (PDF code 30-1483), corresponding to space group R-3H. The crystal structure, as shown in Figure 1b, consists of a sheet of edge-sharing $MnO_6$ octahedra and a layer of Zn cations in a stacking sequence of ⋯Mn-O-Zn-Zn-O-Mn⋯, with the distance between neighboring Mn-O planes to be 4.8 Å. Additionally, there is one vacancy in every seven octahedra in the Mn-O sheet. The $Zn^{2+}$ ions occupy sites above and below the vacant Mn octahedra and are tetrahedrally coordinated to the O atoms of the Mn-O plane. The $Zn^{2+}$ ions can move toward the vacancy along the octahedral triple axis and between the interlayer space[46]. The detailed cell parameters derived from the Rietveld analysis are listed in Table S1. The scanning electron microscope (SEM) image shows a nanostructure morphology with a particle size ranging from 100 to 200 nm (Figure 1c), and energy dispersive X-ray spectroscopy (EDS) mappings demonstrate homogeneous distributions of Zn, Mn, and O elements (Figure 1d). The exact composition ($Zn_{1.02}Mn_3O_7$) is derived from the XPS analysis (Figure 1e, Figure S1).

The electronic structure of ZMO shows an energy gap of 1.56 eV (Figure 1f, 1g). Such a relatively small value may benefit the electron conductivity of the compound. The conduction band maximum (CBM) and the valence band minimum (VBM) are dominated by the Mn-3d and O-2p electron states, whereas the Zn-3d electrons are inactive near the valence band top and the conduction band bottom. The empty electron states of Mn-3d in the VBM indicate the redox activity upon discharging the cathode material.

Figure 2a depicts the initial three-cycle CV curves of ZMO at a scan rate of 0.1 mV/s. A reduction peak located at 0.97 V and an oxidation one at 1.53 V versus $Zn/Zn^{2+}$ are observed during the initial scan. Since the first negative scan starts at the open circuit voltage of ~1.36 V and the electrode experiences a gradual activation process, CV profile of the first circle is different from those of subsequent cycles. Similar phenomena occur to the other manganese oxide cathodes reported for AZIBs.[43,47-48] On cathodic sweeping, two reduction peaks present at around 1.09 and 1.37 V, respectively, which may correspond to the electrochemical intercalation of $Zn^{2+}$ into the cathode host accompanying the reduction of Mn (IV) to lower oxidation states. And on the anodic sweeping, two oxidation peaks at around 1.53 and 1.59 V, respectively may be associated with the extraction of $Zn^{2+}$ from the structure and the reinstatement of Mn (IV) state. For pristine ZMO, the existing $Zn^{2+}$ ions sit in the 6c position (in Wyckoff

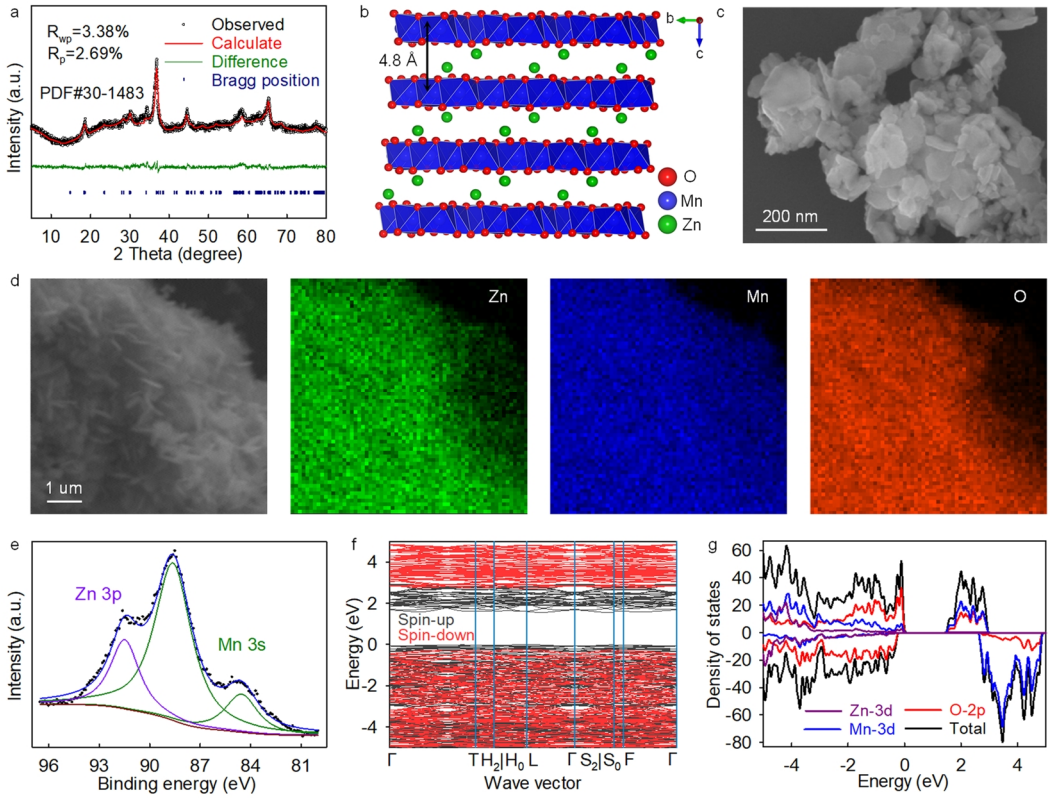


**Figure 1.** Schematic diagram and morphological structure of ZMO. (a) XRD Rietveld refinement. (b) Crystal structure. (c) SEM and (d) SEM-EDS mapping. (e) XPS of Mn 3s. (f) Calculated band structure. (g) The DFT-calculated density of states.




DOI: 10.14102/j.cnki.0254-5861.2022-0092

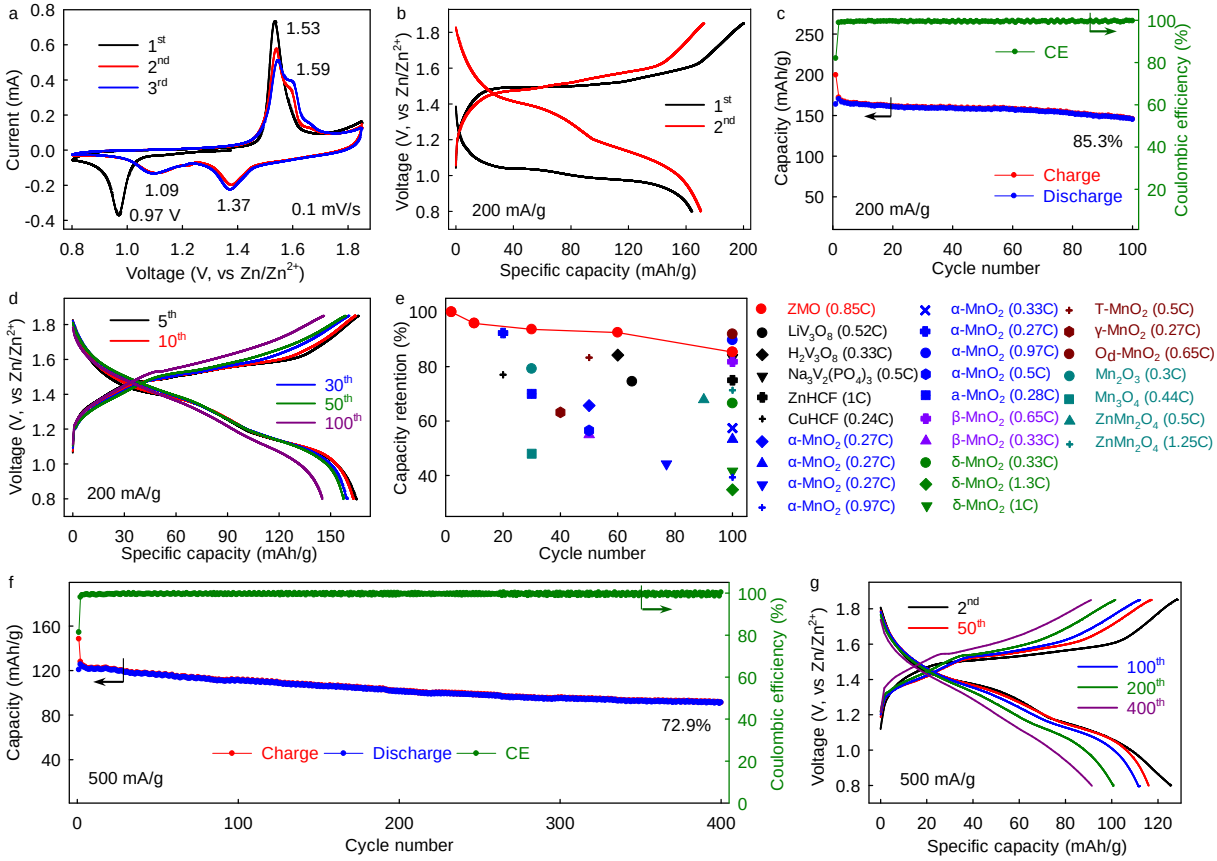


**Figure 2.** Electrochemical performance. (a) CV profiles. (b-d) Galvanostatic charge/discharge voltage profiles and cycling performance at 200 mA/g. (e) Cycling stability comparisons. (f) Cycling performance at 500 mA/g and (g) corresponding voltage profiles.

notation), however, the intercalated $Zn^{2+}$ ions may occupy either the 3b or 18f sites upon the first negative scan. In the subsequent scans, $Zn^{2+}$ ions would exit or enter from/into three inequivalent positions successively, which may lead to significant changes to coordination environments of Mn atoms as all the O atoms surrounding $Zn^{2+}$ ions are from $Mn_3O_7$ sheets, thus giving rise to two redox peaks in the second and third CV curves. Except for the initial profile, CV curves of the followed ones almost overlap with each other, which suggests a highly reversible $Zn^{2+}$ ions extraction/intercalation process.

Figure 2b displays the first two voltage-specific capacity curves at a current density of 200 mA/g. ZMO delivers an initial discharge capacity of 163.7 mAh/g within a voltage window of 0.8 -1.85 V. After two cycles, the specific discharge capacity increases to 170.2 mAh/g and remains stable in the following loops. In addition, the average discharge voltage of ZMO is 1.35 V (vs, $Zn/Zn^{2+}$), giving an energy density of 229.8 Wh/kg based on the mass of active material in the cathode. Figure 2c-g shows the galvanostatic cycling stability and corresponding voltage profiles (200 and 500 mA/g). ZMO is capable of providing an impressive average voltage plateau of 1.35 V, and the capacity retention is 85.3% at the $100^{th}$ cycle with an average coulombic efficiency (CE) of 99.4% at 200 mA/g. The performance at small current densities exceeds those of most manganese-based materials (Figure 2e, Table S2), demonstrating the robust structure of ZMO. At a higher current density of 500 mA/g, capacity retention of 72.9% is obtained over 400 cycles. These excellent properties validate the highly reversible $Zn^{2+}$ ion intercalation chemistry of the ZMO cathode.

Furthermore, ZMO also presents excellent rate capability (Figure 3a, Figure S2). Increasing the current density from 0.1 A/g to 3 A/g, the specific capacities of ZMO are 165.1, 159.4, 136.8, 118.1, 95.3, and 74.8 mAh/g, respectively. The rate performance is superior to a majority of reported Mn-based compounds (Figure 3b, Table S3), and allows for ultrafast charging (73% state of charge in 1.5 min) (Figure S3) and outputting an extremely high power density up to 3510 W/kg at 88 Wh/kg, demonstrating the fast electrochemical reaction kinetics. An in-depth kinetic study of $Zn^{2+}$-(de)intercalation chemistry was carried out by a series of electrochemical characterization methods including the galvanostatic intermittent titration technique (GITT), the electrochemical impedance spectroscopy (EIS), and the rate-scan CV. According to Fick's second law, the following equation is used to calculate the diffusion coefficient of $Zn^{2+}$ ions ($D_{Zn}$):

$$D_{Zn} = (4/\pi\tau) \times [n_M V_M/S]^2 \times [\Delta E_s/\Delta E_t]^2 \quad (1)$$

Where $\tau$ is the duration of a constant current pulse; $n_M$ is the mole number of the electrode; $V_M$ is the mole volume of the electrode; S is the effective contact area between the active material




DOI: 10.14102/j.cnki.0254-5861.2022-0092

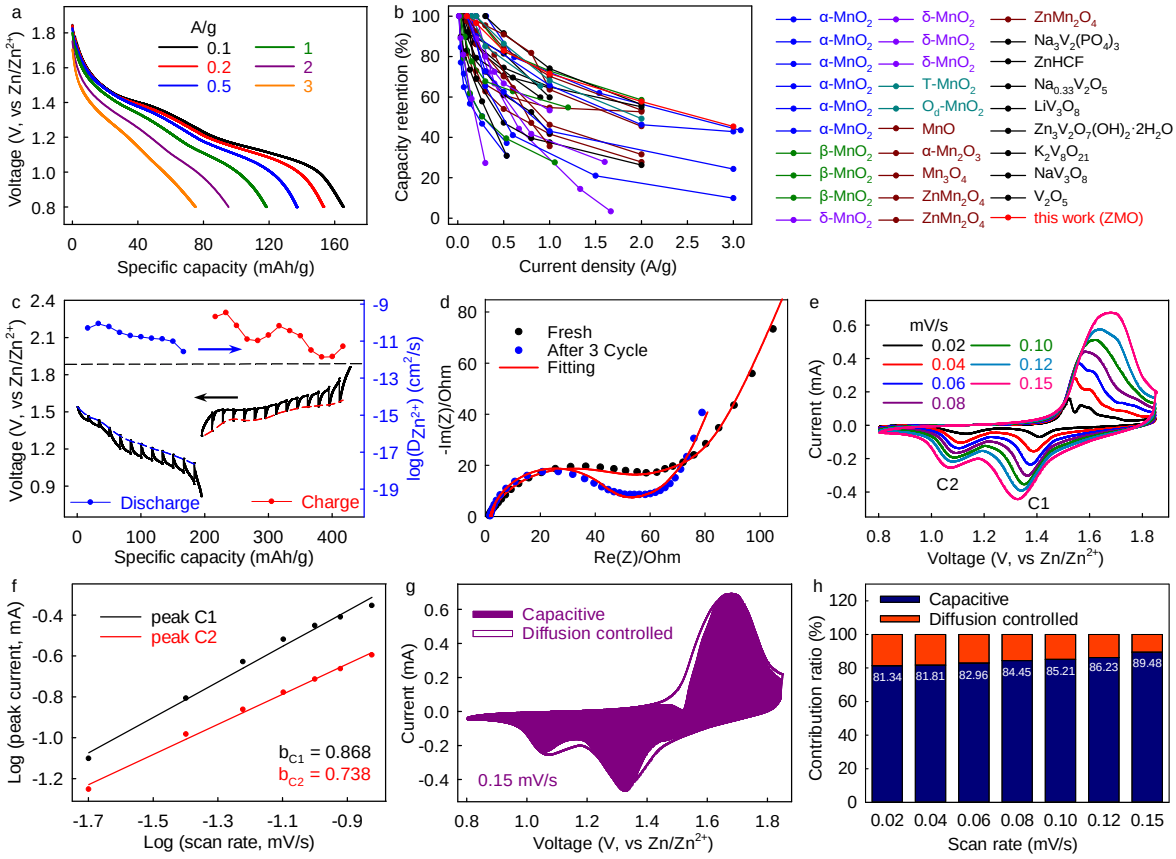


**Figure 3.** Kinetic analysis of $Zn^{2+}$ (de)intercalation within ZMO. (a) Rate capability. (b) Rate performance comparisons. (c) GITT profiles. (d) EIS. (e) Rate-scan CV and (f) Log(peak current) versus log(scan rate) and corresponding b-values. (g) Pseudocapacitive contribution at a scan rate of 0.15 mV/s. (h) The contribution ratio of capacitive and diffusion-controlled processes at different scan rates.

and the electrolyte; and $\Delta E_s$ and $\Delta E_t$ are the change in the steady-state voltage and the overall cell voltage upon applying a current pulse in a single-step GITT experiment, respectively.[49-50] Figure 3c shows the value of $D_{Zn}$ computed from GITT. With the embedding of $Zn^{2+}$ ions, the diffusivity value decreases, and a similar trend also appears in the $Zn^{2+}$ ions exiting process. This phenomenon suggests that $Zn^{2+}$ ion migration becomes more difficult in the second half (de)zincation process. In addition, the large ion diffusion coefficient, i.e., $10^{-10}$-$10^{-12}$ $cm^2/s$, is one to two orders of magnitude higher than the $Li^+$ diffusion coefficients in $LiFePO_4$ and $LiCoO_2$ ($10^{-11}$-$10^{-14}$ $cm^2/s$), allowing for fast ion shuttling. Figure 3d demonstrates the EIS curves for the initial and the third cycles, and the equivalent circuit model (Figure S4) for fitting the EIS data is listed in Table S4. The derived charge transfer resistance ($R_{ct}$) is only 45.08 Ω, which is 5 times lower than that of δ-$MnO_2$ (223 Ω). The ease of $Zn^{2+}$ ion migration in the lattice structure and the facile charge transport at the solid-liquid interface are responsible for its fast-charging capability. Rate scan CV can also provide valuable information on the electrochemical kinetics (Figure 3e). As shown in Figure 3f, based on equation $i = av^b$, the coefficients b corresponding to reduction peaks C1 and C2 can be determined to be 0.868 and 0.738, respectively. The results confirm that the kinetic response of the electrode depends mainly on the capacitive behavior. By integrating the current at each potential at various scanning speeds, the contribution from the capacitor to the total capacity can be determined. The capacitive part at 0.15 mV/s accounts for 89.48% of the total charge storage at the ZMO cathode, as shown in the shaded area of the CV curve in Figure 3g, exceeding those of several recently reported cathode materials for ZIBs (Figure S5). Figure 3h demonstrates the ratio of capacitive contribution at different sweeping rates, which are 81.34%, 81.81%, 82.96%, 84.45%, 85.21%, 86.23%, and 89.48% at 0.02, 0.04, 0.06, 0.08, 0.10, 0.12, and 0.15 mV/s, respectively. According to the above analysis, the fast $Zn^{2+}$ diffusion, and the small charge transfer resistance, together with the dominant capacitive contribution to the specific capacity, are conducive to the achievement of superior fast-charging capability.

To investigate the electrochemical reaction mechanism, ex-situ XRD was used to analyze the crystal structural evolution of the cathode material at different voltage states. Figure 4a displays the voltage profiles of the first two discharge/charge cycles and the diffraction patterns are shown in Figure 4b. At the open-circuit state, the initial structure belongs exactly to $ZnMn_3O_7$. The diffraction peak present at 18.49° can be assigned to the (003) reflection, which is related to the interlayer spacing. When discharged to 0.8 V, the (003) Bragg peak gradually shifts to a higher angle upon the $Zn^{2+}$ embedding, suggesting the decrease




DOI: 10.14102/j.cnki.0254-5861.2022-0092

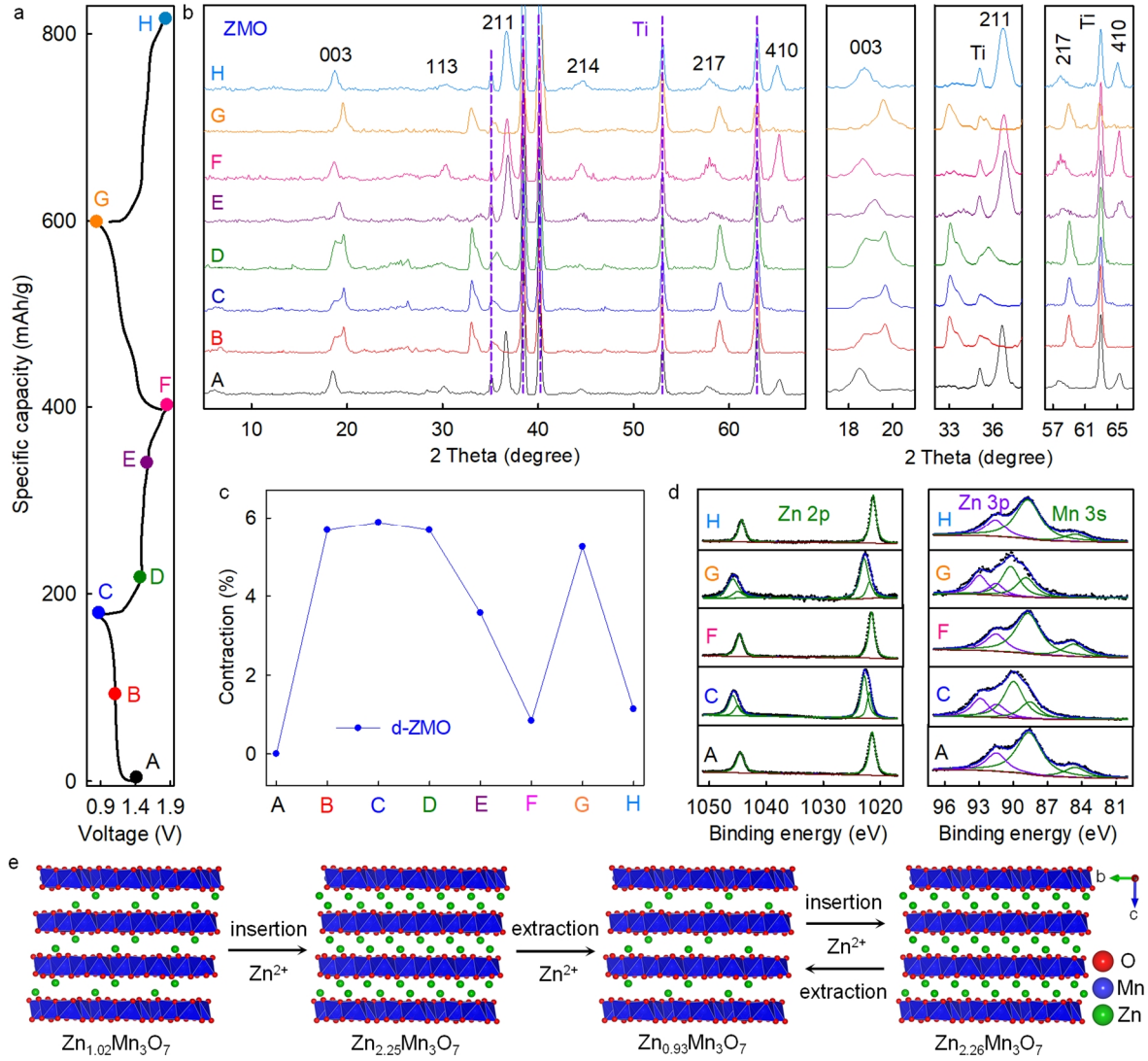


**Figure 4.** Mechanistic study of ZMO cathode. (a) Galvanostatic voltage profiles. (b) Ex-situ XRD analysis. (c) Interlayer spacing evolution derived from XRD. (d) Ex-situ XPS of Zn 2p and Mn 3s. (e) Schematic illustrations of the underlying $Zn^{2+}$ storage mechanism.

of interlayer spacing. And no $Zn_x(OTf)_y(OH)_{2x-y}{\cdot}nH_2O$ was produced as no apparent diffraction peaks present in the interval of 5-15°.[51] Accompanying the disappearance of (211), (214), and (410) reflections, new diffraction peaks located at 33.02° and 58.98° appear as a consequence of minor changes in lattice structure upon the insertion of $Zn^{2+}$ ions. The structural evolution is partly associated with the strong Coulombic interactions between the inserted $Zn^{2+}$ and the lattice $O^{2-}$[52] and the change in the coordination structure of the Mn atom due to the reduction/oxidation reaction. When charged to 1.85 V, the (003) peak gradually shifts back to the low-angle position, indicating the expanding of the associated crystallographic spacing. Moreover, (211), (214), and (410) reflections reappear and the diffraction peaks at 33.02° and 58.98° are absent. Meanwhile, the rightward shifts of the diffraction peaks observed indicate that the lattice shrinks gradually because of the $Zn^{2+}$ embedding, and the lattice expands gradually during the subsequent dezincification process, demonstrating that $Zn^{2+}$ intercalation electrochemistry is highly reversible. It is worth noting that the peak reflected by the (003) crystal plane does not completely return to the initial position, and shifts to a high angle by 0.38°, indicating that irreversible volume contraction occurred, as shown in Figure 4c. This unreversible structure change may be responsible for the decline in specific capacity. Proton intercalation happens to a few Mn-based cathodes, involving the generation of new phases like MnOOH and displaying distinct electrochemical behavior.[53] No H-containing phases are identified from the XRD patterns of the reduced products at various depths of discharge. Moreover, there is no noticeable difference between the first half GITT curve and the second half during discharge. Both results suggest a successive $Zn^{2+}$ ions intercalation process.

Ex-situ XPS further elucidates the $Zn^{2+}$ insertion/extraction process. Figure 4d shows the spectra of Zn 2p and Mn 3s for ZMO. It can be observed from the former that characteristic




DOI: 10.14102/j.cnki.0254-5861.2022-0092

peaks of $Zn^{2+}$ are located at 1021.44 eV (Zn $2p_{3/2}$) and 1044.52 eV (Zn $2p_{1/2}$) in the initial voltage state. When discharged to 0.8 V, the new Zn $2p_{3/2}$ and Zn $2p_{1/2}$ couple appearing at 1022.76 eV and 1045.82 eV, respectively are caused by the additionally embedded $Zn^{2+}$. Apart from the already existing $Zn^{2+}$ in the structure, the embedded $Zn^{2+}$ has a different coordination environment in the host structure.[23] When charged to 1.85 V, the peaks at 1022.76 and 1045.82 eV disappear due to the deintercalation of $Zn^{2+}$ ions. In addition to a Zn 3p peak at 91.48 eV, it can be observed from the Mn 3s spectrum that the initial characteristic peaks of Mn 3s are present at 88.61 and 84.54 eV, respectively. When fully discharged, additional peaks of 92.95 eV (Zn 3p) and 90.01 eV (Mn 3s) appear owing to the newly embedded $Zn^{2+}$ ions and the resulting change in the chemical environment of Mn, respectively. When fully charged, the 92.95 eV (Zn 3p) and 90.01 eV (Mn 3s) peaks disappear because of the removal of $Zn^{2+}$ ions. Prior to cycling, $Zn^{2+}$ ions located at the 6c position in ZMO are tetrahedrally bonded to O atoms. During the first discharge, the intercalated $Zn^{2+}$ ions may occupy either the 3b octahedral or 18f tetrahedral sites. The different coordination environment of $Zn^{2+}$ ions may account for the shifts of the Zn 2p peaks. The consecutive $Zn^{2+}$ ion (de)intercalation also alters coordination environments of Mn atoms considerably, leading to the changes of corresponding Mn 3s peaks. By integrating the peak area of the XPS spectra, the atomic ratios of the cathode at different voltage states are obtained. The schematic demonstration of the underlying reaction mechanism is shown in Figure 4e. The electrochemical reaction in the first discharge is given by

$$Zn_{1.02}Mn_3O_7 + 1.23\ Zn^{2+} + 2.46\ e^- \rightarrow Zn_{2.25}Mn_3O_7 \quad (2)$$

In the first charge, the removal of $Zn^{2+}$ ion can be described by

$$Zn_{2.25}Mn_3O_7 \rightarrow Zn_{0.93}Mn_3O_7 + 1.32\ Zn^{2+} + 2.64\ e^- \quad (3)$$

And the following reversible reaction happened in subsequent discharge/charge processes:

$$Zn_{0.93}Mn_3O_7 + 1.33\ Zn^{2+} + 2.66\ e^- \leftrightarrow Zn_{2.26}Mn_3O_7 \quad (4)$$

## n CONCLUSION

In general, we demonstrate the $Zn^{2+}$ intercalation chemistry in ZMO as a new stable cathode material. The ZMO electrode exhibits a high specific capacity (170.2 mAh/g) and good cycling stability (72.9% capacity retention over 400 cycles). And exceptional rate capability enables ultrafast-charging capability (73% state of charge in 1.5 min) and an ultrahigh power density (3510 W/kg at 88 Wh/kg). The remarkable performance can be attributed to capacitance-dominant behavior, and favorable diffusion of ions, together with the nanostructure morphology, which improves the kinetics of the $Zn^{2+}$ embedding/detachment reaction. Combined with the low cost of ZMO, our results reveal the potential of this novel intercalation chemistry for application in the next generation of ZIBs.

## n EXPERIMENTAL

**Preparation of ZMO.** ZMO was synthesized by a simple sol-gel method combined with ion-exchange modulation. Firstly, we synthesize sodium-containing precursors prior to cation exchange by the aqueous solution method. In a typical synthesis procedure, 63.6 mmol $Mn(CH_3COO)_2$ and 63.6 mmol $NaNO_3$ were dissolved in an appropriate amount of deionized water. The solution was vigorously stirred and dried at 100 °C. Then, the brown powder was obtained. Secondly, the resultant powder was calcined at 400 °C in the air for 7 h to obtain the sodium-containing precursor. Subsequently, the precursor was added to a 300 mL 1.0 mol $L^{-1}$ $ZnSO_4$ solution with continuous stirring for 24 h. Besides, Zn-birnessite was obtained by pouring the slurry into a 100 mL hydrothermal reactor and heat-treatment at 160 °C for 24 h. After cooling down, the product was washed thoroughly with plenty of distilled water and dried in a vacuum oven overnight at 80 °C. Finally, the sample was heated at 280 °C for 1 h.

**Materials Characterization.** Powder X-ray diffraction (XRD) characterizations were performed on the Rigaku Ultima IV power X-ray diffractometer with the Cu-Ka radiation at a voltage of 40 kV and a current of 40 mA. The microscopic morphology of the sample was observed on a scanning electron microscope (SEM, Hitachi SU-8010). Inductively coupled plasma atomic emission spectroscopy measurement was performed on an ICP-OES spectrometer (HORIBA Jobin Yvon, Ultima2). Thermogravimetric analysis (TGA) was conducted on Netzsch STA449F3 with a heating rate of 5 °C/min under airflow. X-ray photoelectron spectroscopy (XPS) was recorded on ESCALAB 250Xi. For ex-situ XRD and XPS analyses, the batteries were disassembled at certain discharge/charge states and the cathodes were washed three times with deionized water before tests.

**Electrochemical Measurements.** Cathodes were performed with CR2032 coin-type cells. To obtain a homogeneous black slurry, active material (ZMO), conductive carbon black (Super P Carbon), and polyvinylidene fluoride (PVDF) were mixed with a weight ratio of 7:2:1 using N-methyl-2-pyrrolidine (NMP) as a solvent. After stirring at 800 rpm for 10 h, the electrode slurry was evenly coated on titanium foil with a loading mass of 1.5 mg $cm^{-2}$ and placed in a vacuum oven at 80 °C for 12 h. A 3 M $Zn(CF_3SO_3)_2$ with 0.3 M $Mn(CF_3SO_3)_2$ aqueous solution was used as the electrolyte. CR2032 coin-type cells were assembled by using zinc foils and Whatman glass fiber as the anode and separator, respectively.

Cyclic voltammetry (CV) test was conducted on a CHI660E electrochemical workstation (Shanghai Chenhua, China) with a voltage range of 0.8-1.85 V (vs, $Zn/Zn^{2+}$) at a scan rate of 0.1 mV $s^{-1}$. Galvanostatic discharge/charge profiles in the voltage range of 0.8-1.85 V (vs, $Zn/Zn^{2+}$) were recorded on a LAND-CT2011A battery-testing instrument at room temperature. The calculation of specific capacity was based on the mass of the initial ZMO. Galvanostatic intermittent titration technique (GITT) was performed on LAND-CT2011A battery-testing instrument. Electrochemical impedance spectroscopy (EIS) was measured on the Bio-Logic SP-300 electrochemical workstation at a frequency ranging from 10 mHz to 100 kHz with an AC voltage of 10 mV.

## n ACKNOWLEDGEMENTS

This work was supported by the Fujian Science and Technology Key Project (No. 2021H0042).




DOI: 10.14102/j.cnki.0254-5861.2022-0092

## AUTHOR INFORMATION

Corresponding author. Email: wzdeng@fjirsm.ac.cn (W. Deng)

## COMPETING INTERESTS

The authors declare no competing interests.

## ADDITIONAL INFORMATION

Supplementary information is available for this paper at http://manu30.magtech.com.cn/jghx/EN/10.14102/j.cnki.0254-5861.2022-0092

For submission: https://mc03.manuscriptcentral.com/cjsc

## REFERENCES

(1) Armand, M.; Tarascon, J.-M. Building better batteries. *Nature* **2008**, 451, 652-657.

(2) Dunn, B.; Kamath, H.; Tarascon, J. M. Electrical energy storage for the grid: a battery of choices. *Science* **2011**, 334, 928-935.

(3) Larcher, D.; Tarascon, J. M. Towards greener and more sustainable batteries for electrical energy storage. *Nat. Chem*. **2015**, 7, 19-29.

(4) Hosenuzzaman, M.; Rahim, N. A.; Selvaraj, J.; Hasanuzzaman, M.; Malek, A. B. M. A.; Nahar, A. Global prospects, progress, policies, and environmental impact of solar photovoltaic power generation. *Renew. Sust. Energ. Rev*. **2015**, 41, 284-297.

(5) Liu, T. C.; Pan, F.; Amine, K. Prospect and reality of concentration gradient cathode of lithium-ion batteries. *Chin. J. Struct. Chem*. **2020**, 39, 11-15.

(6) Liu, S.; Kang, L.; Kim, J. M.; Chun, Y. T.; Zhang, J.; Jun, S. C. Recent advances in vanadium-based aqueous rechargeable zinc-ion batteries. *Adv. Energy Mater*. **2020**, 10, 2000477.

(7) Liu, Y.; Zhu, Y.; Cui, Y. Challenges and opportunities towards fast-charging battery materials. *Nat. Energy* **2019**, 4, 540-550.

(8) Jin, J.; Wu, L.; Huang, S.; Yan, M.; Wang, H.; Chen, L.; Hasan, T.; Li, Y.; Su, B.-L. Hierarchy design in metal oxides as anodes for advanced lithium-ion batteries. *Small Methods* **2018**, 2, 1800171.

(9) Fang, G.; Zhou, J.; Pan, A.; Liang, S. Recent advances in aqueous zinc-ion batteries. *ACS Energy Lett*. **2018**, 3, 2480-2501.

(10) Song, M.; Tan, H.; Chao, D.; Fan, H. J. Recent advances in Zn-ion batteries. *Adv. Funct. Mater*. **2018**, 28, 1802564.

(11) Chen, L. N.; Yan, M. Y.; Mei, Z. W.; Mai, L. Q. Research progress and prospect of aqueous zinc-ion battery. *J. Inorg. Mater*. **2017**, 32, 225.

(12) Ming, J.; Guo, J.; Xia, C.; Wang, W.; Alshareef, H. N. Zinc-ion batteries: materials, mechanisms, and applications. *Mater. Sci. Eng. R Rep*. **2019**, 135, 58-84.

(13) Zhang, Y.; Wan, F.; Huang, S.; Wang, S.; Niu, Z.; Chen, J. A chemically self-charging aqueous zinc-ion battery. *Nat. Commun*. **2020**, 11, 2199.

(14) Blanc, L. E.; Kundu, D.; Nazar, L. F. Scientific challenges for the implementation of Zn-ion batteries. *Joule* **2020**, 4, 771-799.

(15) Zhu, K.; Wu, T.; Huang, K. $NaCa_{0.6}V_6O_{16}\cdot 3H_2O$ as an ultra-stable cathode for Zn-ion batteries: the roles of pre-Inserted dual-cations and structural water in $V_3O_8$ layer. *Adv. Energy Mater*. **2019**, 9, 1901968.

(16) Shin, J.; Choi, D. S.; Lee, H. J.; Jung, Y.; Choi, J. W. Hydrated intercalation for high-performance aqueous zinc-ion batteries. *Adv. Energy Mater*. **2019**, 9, 1900083.

(17) Yang, Y.; Tang, Y.; Fang, G.; Shan, L.; Guo, J.; Zhang, W.; Wang, C.; Wang, L.; Zhou, J.; Liang, S. $Li^+$ intercalated $V_2O_5\cdot nH_2O$ with enlarged layer spacing and fast ion diffusion as an aqueous zinc-ion battery cathode. *Energy Environ. Sci*. **2018**, 11, 3157-3162.

(18) Xia, C.; Guo, J.; Lei, Y.; Liang, H.; Zhao, C.; Alshareef, H. N. Rechargeable aqueous zinc-ion battery based on porous framework zinc pyrovanadate intercalation cathode. *Adv. Mater*. **2018**, 30, 1705580.

(19) Pang, Q.; Sun, C. L.; Yu, Y. H.; Zhao, K. N.; Zhang, Z. Y.; Voyles, P. M.; Chen, G.; Wei, Y. J.; Wang, X. D. $H_2V_3O_8$ nanowire/graphene electrodes for aqueous rechargeable zinc-ion batteries with high rate capability and large capacity. *Adv. Energy Mater*. **2018**, 8, 1800144.

(20) Hu, P.; Zhu, T.; Wang, X.; Wei, X.; Yan, M.; Li, J.; Luo, W.; Yang, W.; Zhang, W.; Zhou, L.; Zhou, Z.; Mai, L. Highly durable $Na_2V_6O_{16}\cdot 1.63H_2O$ nanowire cathode for aqueous zinc-ion battery. *Nano Lett*. **2018**, 18, 1758-1763.

(21) Cai, Y.; Liu, F.; Luo, Z.; Fang, G.; Zhou, J.; Pan, A.; Liang, S. Pilotaxitic $Na_{1.1}V_3O_{7.9}$ nanoribbons/graphene as high-performance sodium-ion battery and aqueous zinc-ion battery cathode. *Energy Storage Mater*. **2018**, 13, 168-174.

(22) Hu, P.; Yan, M.; Zhu, T.; Wang, X.; Wei, X.; Li, J.; Zhou, L.; Li, Z.; Chen, L.; Mai, L. $Zn/V_2O_5$ aqueous hybrid-ion battery with high voltage platform and long cycle life. *ACS Appl. Mater. Interfaces* **2017**, 9, 42717-42722.

(23) Kundu, D.; Adams, B. D.; Duffort, V.; Vajargah, S. H.; Nazar, L. F. A high-capacity and long-life aqueous rechargeable zinc battery using a metal oxide intercalation cathode. *Nat. Energy* **2016**, 1, 16119.

(24) Li, Q.; Ma, K.; Hong, C.; Yang, Z.; Qi, C.; Yang, G.; Wang, C. High-voltage K/Zn dual-ion battery with 100,000-cycles life using zero-strain ZnHCF cathode. *Energy Storage Mater*. **2021**, 42, 715-722.

(25) Deng, W. J.; Li, Z. G.; Ye, Y. K.; Zhou, Z. Q.; Li, Y. B.; Zhang, M.; Yuan, X. R.; Hu, J.; Zhao, W. G.; Huang, Z. Y.; Li, C.; Chen, H. B.; Zheng, J. X.; Li, R. $Zn^{2+}$ induced phase transformation of $K_2MnFe(CN)_6$ boosts highly stable zinc-ion storage. *Adv. Energy Mater*. **2021**, 11, 2003639.

(26) Zhang, Q.; Li, C.; Li, Q.; Pan, Z.; Sun, J.; Zhou, Z.; He, B.; Man, P.; Xie, L.; Kang, L.; Wang, X.; Yang, J.; Zhang, T.; Shum, P. P.; Li, Q.; Yao, Y.; Wei, L. Flexible and high-voltage coaxial-fiber aqueous rechargeable zinc-ion battery. *Nano Lett*. **2019**, 19, 4035-4042.

(27) Yang, Q.; Mo, F.; Liu, Z.; Ma, L.; Li, X.; Fang, D.; Chen, S.; Zhang, S.; Zhi, C. Activating C-coordinated iron of iron hexacyanoferrate for Zn hybrid-ion batteries with 10000-cycle lifespan and superior rate capability. *Adv. Mater*. **2019**, 31, e1901521.

(28) Liu, Z.; Pulletikurthi, G.; Endres, F. A prussian blue/zinc secondary battery with a bio-ionic liquid-water mixture as electrolyte. *ACS Appl. Mater. Interfaces* **2016**, 8, 12158-64.

(29) Gupta, T.; Kim, A.; Phadke, S.; Biswas, S.; Luong, T.; Hertzberg, B. J.; Chamoun, M.; Evans-Lutterodt, K.; Steingart, D. A. Improving the cycle life of a high-rate, high-potential aqueous dual-ion battery using hyper-dendritic zinc and copper hexacyanoferrate. *J. Power Sources* **2016**, 305, 22-29.

(30) Guduru, R. K.; Icaza, J. C. A brief review on multivalent intercalation batteries with aqueous electrolytes. *Nanomaterials* **2016**, 6, 41.

(31) Zhang, L.; Chen, L.; Zhou, X.; Liu, Z. Towards high-voltage aqueous metal-ion batteries beyond 1.5 V: The zinc/zinc hexacyanoferrate system. *Adv. Energy Mater*. **2015**, 5, 1400930.

(32) Naveed, A.; Yang, H.; Yang, J.; Nuli, Y.; Wang, J. Highly reversible and rechargeable safe Zn batteries based on a triethyl phosphate electrolyte. *Angew. Chem. Int. Ed*. **2019**, 58, 2760-2764.

(33) Wan, F.; Niu, Z. Design strategies for vanadium-based aqueous

  
DOI: 10.14102/j.cnki.0254-5861.2022-0092

zinc-ion batteries. *Angew. Chem. Int. Ed*. **2019**, 58, 16358-16367.
(34) Xu, C.; Li, B.; Du, H.; Kang, F. Energetic zinc-ion chemistry: the rechargeable zinc-ion battery. *Angew. Chem. Int. Ed*. **2012**, 51, 933-935.
(35) He, P.; Chen, Q.; Yan, M.; Xu, X.; Zhou, L.; Mai, L.; Nan, C.-W. Building better zinc-ion batteries: a materials perspective. *EnergyChem* **2019**, 1, 100022.
(36) Konarov, A.; Voronina, N.; Jo, J. H.; Bakenov, Z.; Sun, Y. K.; Myung, S. T. Present and future perspective on electrode materials for rechargeable zinc-ion batteries. *ACS Energy Lett*. **2018**, 3, 2620-2640.
(37) Li, C.; Zhang, X.; He, W.; Xu, G.; Sun, R. Cathode materials for rechargeable zinc-ion batteries: from synthesis to mechanism and applications. *J. Power Sources* **2020**, 449, 227596.
(38) Zhao, Q. H.; Ding, S. X.; Song, A. Y.; Qin, R. Z.; Pan, F. Tuning structure of manganese oxides to achieve high-performance aqueous Zn batteries. *Chin. J. Struct. Chem*. **2020**, 39, 388-394.
(39) Li, W. J.; Han, C.; Wang, Y.; Liu, H. K. Structural modulation of manganese oxides for zinc-ion batteries. *Chin. J. Struct. Chem*. **2020**, 39, 31-35.
(40) Wang, J.; Wang, J.-G.; Liu, H.; You, Z.; Wei, C.; Kang, F. Electrochemical activation of commercial MnO microsized particles for high-performance aqueous zinc-ion batteries. *J. Power Sources* **2019**, 438, 226951.
(41) Hao, J.; Mou, J.; Zhang, J.; Dong, L.; Liu, W.; Xu, C.; Kang, F. Electrochemically induced spinel-layered phase transition of $Mn_3O_4$ in high performance neutral aqueous rechargeable zinc battery. *Electrochim. Acta* **2018**, 259, 170-178.
(42) Jiang, B.; Xu, C.; Wu, C.; Dong, L.; Li, J.; Kang, F. Manganese sesquioxide as cathode material for multivalent zinc-ion battery with high capacity and long cycle life. *Electrochim. Acta* **2017**, 229, 422-428.
(43) Zhang, N.; Cheng, F.; Liu, Y.; Zhao, Q.; Lei, K.; Chen, C.; Liu, X.; Chen, J. Cation-deficient spinel $ZnMn_2O_4$ cathode in $Zn(CF_3SO_3)_2$ electrolyte for rechargeable aqueous Zn-ion battery. *J. Am. Chem. Soc*. **2016**, 138, 12894-12901.
(44) Pan, H.; Shao, Y.; Yan, P.; Cheng, Y.; Han, K. S.; Nie, Z.; Wang, C.; Yang, J.; Li, X.; Bhattacharya, P.; Mueller, K. T.; Liu, J. Reversible aqueous zinc/manganese oxide energy storage from conversion reactions. *Nat. Energy* **2016**, 1, 16039.
(45) Zhang, N.; Cheng, F.; Liu, J.; Wang, L.; Long, X.; Liu, X.; Li, F.; Chen, J. Rechargeable aqueous zinc-manganese dioxide batteries with high energy and power densities. *Nat. Commun*. **2017**, 8, 405.
(46) Post, J. E.; Appleman, D. E. Chalcophanite, $ZnMn_3O_7{\cdot}3H_2O$: new crystal-structure determinations. *Am. Mineral*. **1988**, 73, 1401-1404.
(47) Lee, B.; Lee, H. R.; Kim, H.; Chung, K. Y.; Cho, B. W.; Oh, S. H. Elucidating the intercalation mechanism of zinc-ions into alpha-$MnO_2$ for rechargeable zinc batteries. *Chem. Commun*. **2015**, 51, 9265-9268.
(48) Alfaruqi, M. H.; Mathew, V.; Gim, J.; Kim, S.; Song, J.; Baboo, J. P.; Choi, S. H.; Kim, J. Electrochemically induced structural transformation in a γ-$MnO_2$ cathode of a high capacity zinc-ion battery system. *Chem. Mater*. **2015**, 27, 3609-3620.
(49) Weppner, W.; Huggins, R. A. Determination of the kinetic parameters of mixed-conducting electrodes and application to the system $Li_3Sb$. *J. Electrochem. Soc*. **1977**, 12, 1569–1578.
(50) Mao, Z.; Farkhondeh, M.; Pritzker, M.; Fowler, M.; Chen, Z. Dynamics of a blended lithium-ion battery electrode during galvanostatic intermittent titration technique. *Electrochim. Acta* **2016**, 222, 1741-1750.
(51) Wang, L.; Huang, K. W.; Chen, J.; Zheng, J. Ultralong cycle stability of aqueous zinc-ion batteries with zinc vanadium oxide cathodes. *Sci. Adv.* **2019**, 5, eaax4279.
(52) Zhang, G.; Wu, T.; Zhou, H.; Jin, H.; Liu, K.; Luo, Y.; Jiang, H.; Huang, K.; Huang, L.; Zhou, J. Rich alkali ions preintercalated vanadium oxides for durable and fast zinc-ion storage. *ACS Energy Lett*. **2021**, 6, 2111-2120.
(53) Sun, W.; Wang, F.; Hou, S.; Yang, C.; Fan, X.; Ma, Z.; Gao, T.; Han, F.; Hu, R.; Zhu, M.; Wang, C. Zn/$MnO_2$ battery chemistry with $H^+$ and $Zn^{2+}$ coinsertion. *J. Am. Chem. Soc.* **2017**, 139, 9775-9778.

Received: April 21, 2022
Accepted: May 12, 2022
Published: May 20, 2022




DOI: 10.14102/j.cnki.0254-5861.2022-0092